Journal of
Materials Chemistry A

Materials for energy and sustainability

## Accepted Manuscript

This article can be cited before page numbers have been issued, to do this please use: S. V. Talande, A. Bakandritsos, L. Zdražil, P. Jakubec, E. Mohamadi, O. Tomanec, M. Otyepka, V. Presser, R. Zboril and J. Tucek, *J. Mater. Chem. A*, 2020, DOI: 10.1039/D0TA06998A.




ROYAL SOCIETY OF CHEMISTRY

rsc.li/materials-a

# Pinning ultrasmall greigite nanoparticles on graphene for effective transition-metal-sulfide supercapacitors in an ionic liquid electrolyte†

Smita Talande,[a,b] Aristides Bakandritsos,[a,c*] Lukáš Zdražil,[a,d] Petr Jakubec,[a] Elmira Mohammadi,[a] Ondřej Tomanec,[a] Michal Otyepka,[a] Volker Presser,[e,f] Radek Zbořil,[a,c,g] Jiří Tuček[h,*]

[a] *Regional Centre of Advanced Technologies and Materials, Faculty of Science, Palacký University, Šlechtitelů 27, 783 71, Olomouc, Czech Republic*

[b] *Department of Experimental Physics, Faculty of Science, Palacký University, 17. listopadu 1192/12, 779 00 Olomouc, Czech Republic*

[c] *Nanotechnology Centre, VŠB–Technical University of Ostrava, 17. listopadu 2172/15, 708 00 Ostrava-Poruba, Czech Republic*

[d] *Department of Physical Chemistry, Faculty of Science, Palacký University, 17. listopadu 1192/12, 779 00 Olomouc, Czech Republic*

[e] *Department of Materials Science & Engineering, Saarland University, Campus D2 2, 66123 Saarbrücken, Germany*

[f] *INM - Leibniz Institute for New Materials, Campus D2 2, 66123 Saarbrücken, Germany*

[g] Institute of Organic Chemistry and Biochemistry, Academy of Sciences of the Czech Republic, v.v.i., Flemingovo nám. 2, 16610 Prague 6, Czech Republic

[h] *Department of Mathematics and Physics, Faculty of Electrical Engineering and Informatics, University of Pardubice, náměstí Čs. legií 565, 530 02 Pardubice, Czech Republic*

** Corresponding authors' e-mail addresses*: a.bakandritsos@upol.cz; jiri.tucek@upce.cz

View Article Online
DOI: 10.1039/D0TA06998A





## Abstract

To meet the future demands for off-grid power, high-performance electrochemical energy storage based on earth-abundant materials is essential. Supercapacitors are attractive in this sense due to their sustainable carbon-based architecture, rapid charging/discharging, and long cycle-life in comparison to battery chemistries. However, hybridizing carbon electrodes with inorganic phases is intensively explored in supercapacitor research to mitigate their low energy content. Iron sulfides are attractive because they are non-toxic and composed of earth-abundant elements, but, despite their hydrophobic nature, they have only been studied in aqueous electrolytes, limiting the energy content due to the narrow voltage stability window of water. Here, exploiting a rapid growth method and a highly functionalized graphene support, we strongly immobilized greigite ($Fe_3S_4$) nanoparticles with an ultrasmall size which could not be attained in the absence of graphene. The respective supercapacitor cell was found significantly more electroactive in the ionic liquid electrolyte than in water, boosting the energy content. Furthermore, greigite has high conductivity and fast surface faradic reactions due to the enzyme-mimicking triple redox state of its thiocubane basic structural unit. Thus, fully reversible and fast redox processes in the expanded voltage-window of the ionic liquid also ascribed excellent rate capability, cycling stability, and power. The work demonstrates a pathway, not previously explored, whereby greigite/graphene hybrids can surpass in these aspects top-rated supercapacitor materials.

## Keywords:

ultracapacitors; electric double-layer capacitors; cyanogaphene; greigite; energy density

## 1. Introduction

Due to the rapid development of mobile electronics for communication, processing, and accessing information, for remote networking and device co-operation for the internet-of-things, there is a growing demand for off-grid energy storage and supply.[1–3] Supercapacitors are promising energy storage technology due to their rapid charging/discharging, excellent cycling stability, high power, low cost, and sustainable carbon-based electrochemistry.[2,4] However, they suffer from low energy content, which limits their wider applicability.[3,5] To this end, efforts have been focused on developing hybrid electrode materials[6–11] composed of carbon allotropes[12,13] and nanostructured transition metal oxides (e.g., FeOOH,[14,15] $CuCo_2O_4$,[16] $MnO_2$, and metal-organic frameworks[6,17,18]) to take advantage of the ability of the latter to boost charge storage through redox reactions. Carbon components or supports compensate for the usually poor conductivity of metal oxides improving the electronic and ionic transport throughout the electrode. Electrochemical activity is further promoted in such hybrids by hindering the aggregation of the inorganic nanostructures, which can then offer higher accessibility to active surface sites for charge storage. Conductive and functional carbon allotropes, such as graphene and reduced graphene oxide,[11,19] N-doped graphene,[20] and graphdiyne[11,21–23] are an essential part of electrodes.

Recently, hybrids with transition metal sulfides (TMS; such as cobalt,[24,25] iron,[26,27] and sulfides of other metals,[28–31] have also attracted attention due to their higher conductivity than transition metal oxides.[32] Sulfur has a lower electronegativity than oxygen, and the Fe-S bond has a more covalent character than the Fe-O bond, thus imparting to TMS better charge transport,[32] smaller bandgap,[33] and lower volume expansion during charging.[27] The operation of such electroactive materials has been dominantly studied in aqueous KOH

electrolytes[24,27,32] (Table S1, ESI†) to exploit the high ion mobility in water, the $OH^-$ mediated redox chemistry, as well as the suppressed sulfur losses as polysulfides in the aqueous electrolytes.[34] However, the same properties of sulfur, which improve the conductivity of TMS, reduce their wetting for aqueous electrolytes.[35] Sulfurization is used to induce phase separation, and recovery by flotation of oxide minerals in aqueous processes,[36] and thiocubane units ($Fe_4S_4$) are hosted on the hydrophobic pockets of enzymes as redox and charge-transfer mediators.[37] Furthermore, operation in aqueous electrolytes significantly limits the voltage window ($V$), and thus the energy content, since the latter scales with $V^2$.[5,38,39] Interestingly, greigite ($Fe_3S_4$), with the highest conductivity among TMS and elegant redox chemistry due to its thiocubane basic structural unit,[40] has not been previously explored.

In this work, we report on the rapid (5 min) synthesis and efficient operation of a graphene/$Fe_3S_4$-based electrode material in a non-aqueous, high potential-window electrolyte, an aspect that has previously been overlooked for TMS-based supercapacitor electrodes. More specifically, a cyanographene/$Fe_3S_4$ hybrid ($GCNFe_3S_4$) was developed, comprising ultrasmall (2-3 nm) $Fe_3S_4$ nanoparticles. The nanoparticles were grafted very firmly to the GCN backbone, as indicated by the large increase of the temperature during thermal analysis, at which sulfur losses took place after immobilization on GCN, in comparison to pure $Fe_3S_4$. $GCNFe_3S_4$ delivered 8.5 Wh $kg^{-1}$ at 3.2 kW $kg^{-1}$ (at total-electrode mass level), surpassing all TMS-based supercapacitors, such as the metal-organic-framework-derived $Co_9S_8$ nanoparticles embedded on carbon[24] with a specific energy of 6.5 Wh $kg^{-1}$ at a specific power of 2.2 kW $kg^{-1}$, ternary transition metal sulfides embedded in graphene nanosheets[29] with 1.9 Wh $kg^{-1}$ at 0.3 kW $kg^{-1}$, FeS immobilized on reduced graphene oxide against a $Ni(OH)_2$ electrode[41] with 8.1 Wh $kg^{-1}$ at 3 kW $kg^{-1}$ and many more metal sulfide systems described in detail in Table S1, ESI†. Interestingly, also transition metal oxide-based supercapacitors such

View Article Online
DOI: 10.1039/D0TA06998A

as hematite quantum dots anchored of three-dimensional graphene-like framework[42] with a specific energy of 6.7 Wh $kg^{-1}$ at a power of 2.2 kW $kg^{-1}$, porous $Mn_3O_4$//$Fe_3O_4$ electrodes (Ref. [43]) with an energy of 3.5 Wh $kg^{-1}$ at a power of 3.5 kW $kg^{-1}$ and graphene-supported $Fe_2O_3$ (Ref. [44]) were also not superior to the GCN$Fe_3S_4$ cell (including in the metrics the mass of the current collectors). GCN$Fe_3S_4$ also delivered an ultrahigh energy density of 49 mWh $cm^{-3}$ at 2.4 W $cm^{-3}$, outperforming not only previous TMS-based supercapacitors,[45,46] but several other top-rated materials.[47–52] The cycle-life and rate performance were also exceptional due to the rapid and reversible surface redox processes, facilitated from the triple redox-state ability of the $Fe_3S_4$ units, firmly immobilized on the conductive and highly functionalized GCN backbone.

## 2. Experimental section

### 2.1. Reagents and materials

Graphite fluoride, $FeCl_3$ anhydrous, NaCN, thiourea, ethylene glycol, $Na_2SO_4$, poly(vinylidene fluoride), N-methyl-2-pyrrolidone, 1-ethyl-3-methylimidazolium tetrafluoroborate ($EMIMBF_4$), battery-grade 1 M $LiPF_6$ in propylene carbonate, 1 M $LiPF_6$ in ethylene carbonate, and in dimethyl carbonate, were purchased from Sigma-Aldrich. Acetone (pure), ethanol (absolute), amine-free N,N-dimethylformamide (DMF), KOH were purchased from Penta. Carbon black was purchased from AkzoNobel (ketjen black EC600, 1400 $m^2$ $g^{-1}$). Lithium bis(trifluoromethanesulfonyl)imide (LiTFSI) was purchased from TCI. Active carbon (type YP-80F) was obtained from Kuraray. All reagents were used without further purification. Ultrapure water was obtained from Mirae ST Instrument (Esse-UP Analysis, S00005812).

View Article Online
DOI: 10.1039/D0TA06998A





## 2.2. Material synthesis

### *2.2.1. Synthesis of cyanographene (GCN)*

GCN was synthesized as previously reported[53] with minor modifications. Briefly, graphite fluoride (1 g) was dispersed in DMF (60 mL) in a round-bottom glass flask, kept for stirring for 1 d and then sonicated (Bandelin Sonorex, DT 255H type, frequency 35 kHz, power 640 W, effective power 160 W) for 4 h. Then, NaCN (2 g) was added and heated to 130 °C under stirring at 600 rpm; finally, the system was kept at the target temperature for 48 h. After the mixture cooled, the solid was isolated and washed with centrifugation in 15 mL falcons using DMF (2×), acetone (4×), ethanol (4×), and water (4×). In DMF and water, the solid was not properly precipitating, and 1% HCl (0.4 mL) was added in each falcon, which facilitated full precipitation. The precipitate was finally re-dispersed in water and subjected to dialysis until the conductivity of the dispersion was below 150 $\mu S \cdot cm^{-1}$.

### *2.2.2. Synthesis of GCN/$Fe_3S_4$*

A microwave-assisted synthesis was used to prepare cyanogaphene/greigite. $FeCl_3$ (53 mg) and thiourea (82 mg) were dissolved into ethylene glycol (1 mL) separately. In a microwave glass vial, GCN (45 mg) was dispersed in ethylene glycol (3 mL), and the solutions of $FeCl_3$ and thiourea were added dropwise, then 100 µL ultrapure water was added. The mixture was stirred (5 min.) and placed into the microwave reactor (microwave 300, Anton Paar) for 5 min, at 180 °C under stirring (600 rpm). Then, the mixture was purified by rinsing with ethanol.

## 2.3. Materials characterization

X-ray diffraction (XRD) was recorded with an X'Pert PRO MPD (PANalytical) diffractometer in the Bragg-Brentano geometry, Co-$K_\alpha$ radiation (40 kV, 30 mA, $\lambda$ = 0.1789 nm) equipped with an X'Celerator detector and programmable divergence and diffracted beam anti-scatter slits. The step size of the measurements was set at 0.033°. The identification of crystalline phases

View Article Online
DOI: 10.1039/D0TA06998A





was performed using the High Score Plus software (PANalytical) that includes the PDF-4+ database.

Transmission electron microscopy images were obtained with a JEOL 2100 system. High-resolution electron microscopy was performed with an FEI TITAN 60-300 HRTEM microscope with an X-FEG type emission gun, operating at 80 kV. Scanning transmission electron microscopy in high-angle angular dark field mode for elemental mapping on the $GCNFe_3S_4$ sheets was performed with the same microscope. Thermogravimetric analysis (TGA; Netzsch STA 449C Jupiter thermal analyzer) in synthetic air was performed in order to obtain the mass content of the inorganic phase. The TGA instrument was equipped with a QMS 403 Aëolos mass spectrometer for evolved gases (EGA). The measurements in synthetic air (100 $cm^3 \cdot min^{-1}$) were carried out using an open crucible made of α-$Al_2O_3$, from 45 °C to 1000 °C and a heating rate of 10 $K \cdot min^{-1}$. The EGA was focused on m/z 18, 44, 48, and 64 for $H_2O$, $CO_2$, SO, and $SO_2$, respectively. X-ray photoelectron spectroscopy (XPS) was carried out with a PHI VersaProbe II (Physical Electronics) spectrometer using an Al-$K_\alpha$ source (15 kV, 50 W). The obtained data were evaluated with the MultiPak (Ulvac - PHI, Inc.) software package. The photoluminescence spectroscopy measurements were carried out using the FLS980 fluorescence spectrometer (Edinburgh Instruments) equipped with a 450 W xenon arc lamp as the excitation source.

### 2.4. Electrode preparation and electrochemical characterization

A three-electrode open-cell configuration was used for the preliminary electrochemical testing in aqueous 1 M $Na_2SO_4$ electrolyte, a platinum electrode as the counter electrode, and Ag/AgCl as the reference electrode. The samples were deposited on a glassy carbon electrode (GCE). Sample suspension (10 µL, 2 $mg \cdot mL^{-1}$) was drop-coated on GCE and allowed to dry in

View Article Online
DOI: 10.1039/D0TA06998A

the air at room temperature. The measurements were performed using an electrochemical workstation PGSTAT128N (Metrohm Autolab) monitored by NOVA software.

For the preparation of full cell, the active material, carbon black, and poly(vinylidene fluoride) binder in the weight ratio 90:5:5 were dispersed in *N*-methylpyrrolidone to prepare a homogenous slurry. The slurry was deposited on carbon-coated Al foil (purchased from MTI; EQ-CC-Al-18u-260; thickness of 18 µm; mass 3.4 mg·cm$^{-2}$) using a doctor blade. The prepared electrodes were then dried into a vacuum oven (40 mbar) overnight at 60 °C and punched into 18 mm diameter electrodes. The electrodes were tested in different electrolytes 1 M $LiPF_6$ in propylene carbonate (PC), 1 M $LiPF_6$ in ethylene carbonate/dimethyl carbonate, 0.2 M LiTFSI in $EMIMBF_4$ (IL+Li-salt), and 6 M KOH in water. For measurements in 6 M KOH, the paste was coated on a gold current collector. The mass loadings were 0.9 mg·cm$^{-2}$ or 3.5 mg·cm$^{-2}$ for two different supercapacitor cells. Next, the cells were assembled using a PAT-cell testing system (EL-CELL) and tested with a Bio-Logic potentiostat (BCS-810) and BTlab software. Electrochemical impedance spectra were obtained from the full cell devices in the frequency range from 0.01 Hz to 100 kHz with an AC amplitude of 10 mV using the same instrument.

Specific capacitance, specific energy, and specific power were calculated by the equations below:

$$C = 4\frac{I\ \Delta t}{m\Delta V} \text{ in } F\ g^{-1} \quad \text{Eq. 1}$$

$$E = \frac{1CV^2}{8\,3.6}\ in\ Wh\ kg^{-1} \quad \text{Eq. 2}$$

$$P = \frac{3.6\ E}{\Delta t}\ in\ kW\ kg^{-1} \quad \text{Eq. 3}$$

where, $I$ is the applied current, $\Delta t$ is the discharge time in seconds, $\Delta V$ is the operating potential/voltage, $m$ is the active mass in both electrodes. The active mass was used in order to be comparable with literature reports (Table S1, ESI†), which also used active mass metrics.

View Article Online
DOI: 10.1039/D0TA06998A

When performance at total electrode mass level is reported, then the mass term (*m*) in Eq. 1 includes the mass of the current collectors.

The performance was also calculated by using integral equations for non-linear galvanostatic charge-discharge curves, for the sake of more accurate metrics, which are available in Table S3, ESI†.

$$E = \frac{I}{m}\frac{\int V dt}{3.6} \text{ in } F\ g^{-1} \quad \text{Eq.4}$$

where *V* is the operating voltage, and *I/m* is the specific current, and *m* is the mass in both electrodes.

## 3. Results and Discussion

### 3.1. Synthesis and material characterization

The GCN$Fe_3S_4$ hybrid was synthesized using a simple, one-step, and rapid (5 min) microwave-assisted method, affording a ready-to-paste material on 18 μm thick aluminum current collectors. In particular, a GCN dispersion in ethylene glycol was mixed with $FeCl_3$ and thiourea and was processed in a microwave reactor for 5 min at 180°C, readily affording the GCN$Fe_3S_4$ hybrid paste. GCN, prepared as previously reported,[53] is an electronically conductive and densely functionalized graphene-derivative (12-15% degree of functionalization) with nitrile groups, appropriate for binding greigite nanoparticles. This firm bonding could prevent the aggregation of nanoparticles and the restacking of graphene nanosheets. Indeed, a previous microwave synthesis of TMS nanoparticles in the presence of non-functionalized graphene nanosheets[27] afforded particles with a diameter of ca. 40 nm, in contrast to the smaller than 5 nm diameter nanoparticles obtained herein (Fig. 1a). Interestingly, in the absence of GCN, but otherwise under identical synthetic conditions, the $Fe_3S_4$ nanoparticles grew much larger (ca. 40 nm, Fig. S2c), highlighting the key role of GCN. Restricting the dimensions of

pseudocapacitive materials is crucial for suppressing phase changes and for allowing fast surface redox process, not limited by the slow reaction rates of phase transitions typically seen in battery chemistries.[38,54] Furthermore, this new synthetic approach offered a straightforward method for in-situ wet-chemical preparation of graphene/greigite hybrids, unlike other methods requiring hydrothermal,[25] electrochemical or chemical vapor deposition[55] of TMS nanoparticles directly on the current collectors. The direct growth on the current collectors requires their presence in the reaction vessels, which impedes a high-throughput electrode production.

High-resolution transmission electron microscopy (HR-TEM) confirmed the uniform distribution of ultrasmall nanoparticles (Fig. 1a-d) with a mean diameter of 2.2 nm and a standard deviation of 20% (inset in Fig. 1a), appearing as dark spots over the graphene sheet in Fig. 1a. The lattice fringes visible in Fig. 1b,c showed *d*-spacings of 2.5 Å and 3.0 Å, which correspond to the (400) and (311) crystal planes, respectively, of greigite.[56] High-angle annular dark-field scanning transmission electron microscopy (HAADF-STEM, Fig. 1d) indicated that iron (i.e., greigite) completely covered the surface of GCN, evidenced by the bright spots corresponding to metal-rich areas. The elemental mapping via energy-dispersive X-ray spectroscopy (EDX) further corroborated the homogeneous coverage of the GCN flakes with nitrogen and Fe, indicating the uniform functionalization of graphene both with the nitrile groups and the ultrasmall greigite nanoparticles (Fig. 1e-h).

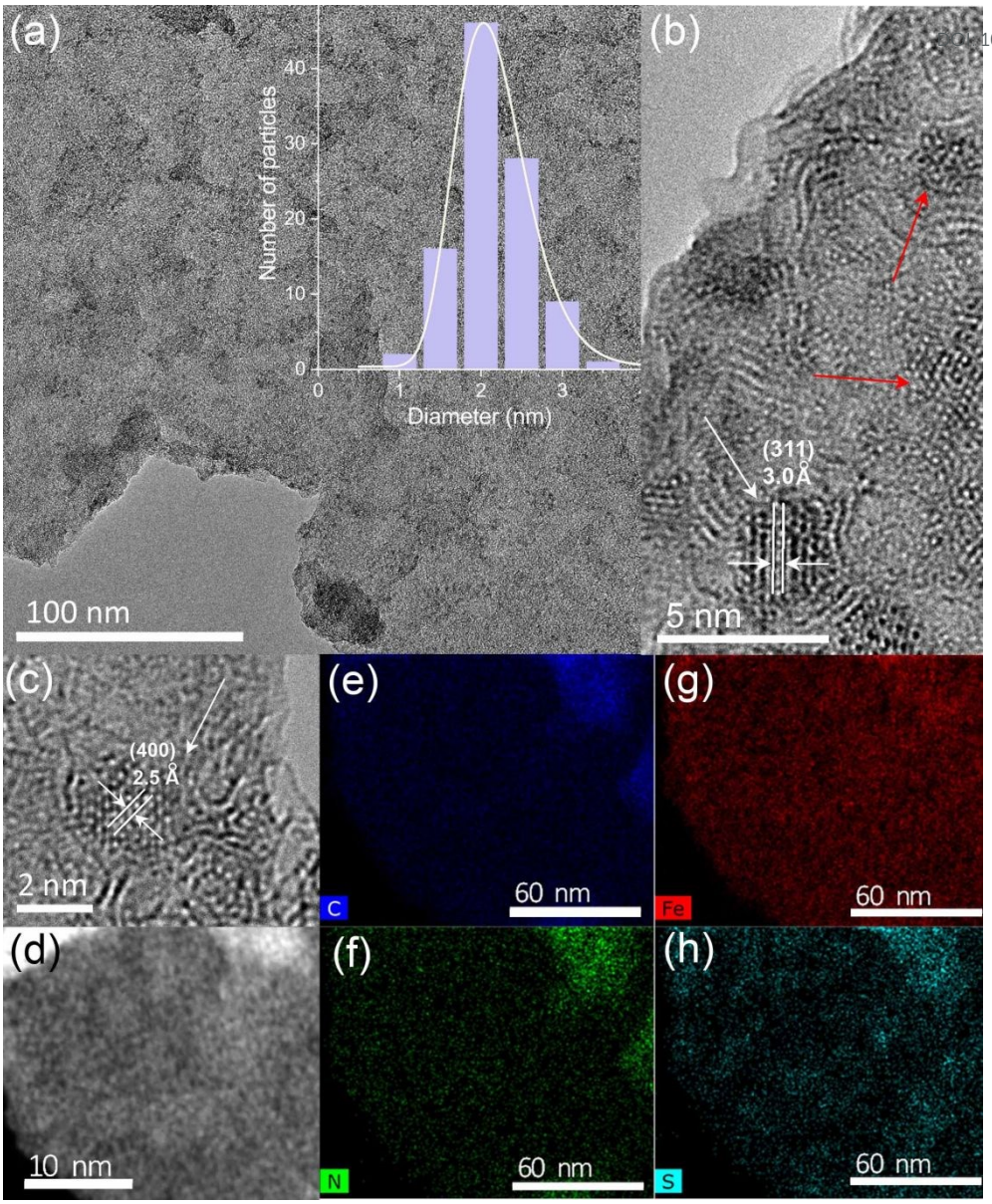


**Fig. 1.** (a-c) Transmission electron micrographs of the GCN$Fe_3S_4$ hybrid material. (d) High-angle annular dark-field scanning transmission electron micrographs and (e-h) corresponding elemental mapping for (e) carbon, (f) nitrogen, (g) iron, and (h) sulfur.

X-ray photoelectron spectroscopy (XPS) confirmed the presence of the carbon, nitrogen, iron, and sulfur in the GCN$Fe_3S_4$ hybrid (Fig. S1, ESI†). The high-resolution X-ray photoelectron emission spectrum of Fe2p (Fig. 2a) showed that iron atoms were in the form of $Fe^{2+/3+}$ ions occupying the octahedral sites (at 710.7 eV representing a mixed 2.5+ valence state ) and $Fe^{3+}$ ( at 724.3 eV) with a binding energy difference of 13.5 eV. These are typical

for the mixed-valence spinel structure of greigite,[57] characterized by the thiocubane basic structural unit, shown in Fig. 2c. There was an apparent lower $Fe^{3+}/Fe^{2+/3+}$ spectral areal ratio of 0.33 compared to the nominal 0.5 ratio, evidencing the presence of surface defects on the ultrasmall nanoparticles. This was also apparent by the irregular outer lattice fringes of the nanoparticles (Fig. 1c), or the presence of nanoparticles without regular fringes at all (Fig. 1b, indicated by red arrows). The spectrum of the S2p region was also deconvoluted with two pairs of doublets (Fig. 2b), reflecting the spin-orbit splitting of $S2p_{3/2}$ and $S2p_{1/2}$ peaks, separated by 1.16 eV.[58] The lower-eV doublet corresponds to $S^{2-}$ (typical for greigite[57]), and the high-eV doublet corresponds to $S_2^{2-}$. The presence of these $S_2^{2-}$ species ($S^{1-}$-$S^{1-}$) along with the increased content in $Fe^{2+}$ is also attributed to the very small size and defect-rich structure of the nanoparticles, whereby a thermodynamically driven redox process of $S^{2-}$ oxidation to $S_2^{2-}$ and respective reduction of $Fe^{3+}$ to $Fe^{2+/3+}$ (thus the lower than nominal $Fe^{3+}/Fe^{2+/3+}$ ratio) probably takes place at the exposed nanoparticles surface.[59]

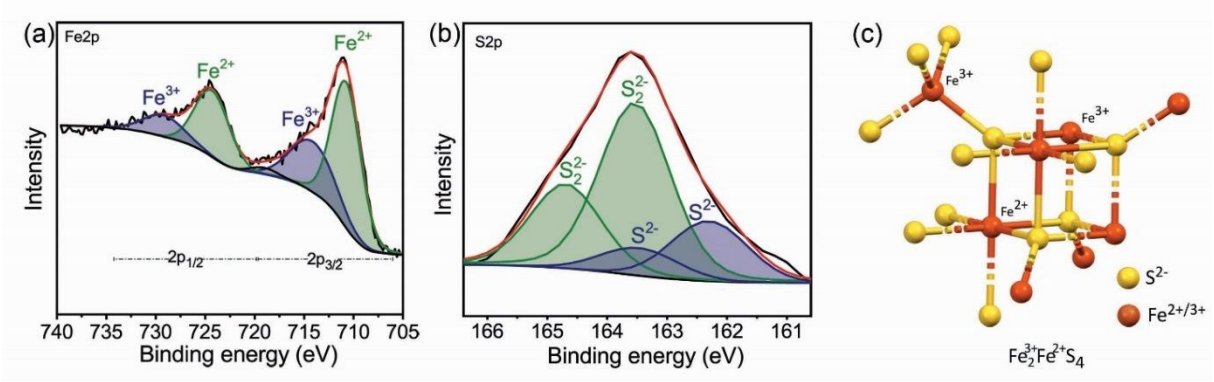


**Fig. 2**. Deconvoluted X-ray photoelectron emission spectra for the (a) iron and (b) sulfur regions of $GCNFe_3S_4$. (c) The basic structural motif of greigite, corresponding to the thiocubane unit (crystallographic database card: amcsd 0000127).

To better highlight the benefits of combining greigite with GCN in terms of properties and electrochemical performance, pure greigite was also prepared with the same method in the absence of GCN. The formation of the greigite lattice was verified by X-ray diffraction (Fig. 3a) in both the absence and presence of GCN during the synthesis. In the X-ray diffractogram of the hybrid material, the (220) reflection from $Fe_3S_4$ at ca. 30° 2θ was hidden by the dominating contribution of the graphene matrix. The content of $Fe_3S_4$ in the hybrid was estimated at about 30 mass%, according to the thermogravimetric analysis in air (TGA, Fig. 3b). The evolved gas analysis showed the emission of SO and $SO_2$ gasses detected, confirming the presence of sulfur in both cases. In pure $Fe_3S_4$, SO and $SO_2$ evolved at 220-280 °C and 345-360 °C, respectively. In the GCN$Fe_3S_4$ hybrid, the SO and $SO_2$ emissions peaked at a significantly higher temperature range (460-495 °C), suggesting the strong interaction between the functionalized graphene matrix and $Fe_3S_4$ nanoparticles. Interestingly, the SO and $SO_2$ release peaked at exactly the same temperature of the GCN decomposition (see the $CO_2$ evolution upon combustion in Fig. S2, ESI†), which supported further the strong binding achieved in the hybrid. In connection to these findings, the role of GCN should be therefore highlighted, since it is endowed with a particularly high functionalization degree of 12-15%,[53] offering abundant binding sites for interacting with the in-situ grown greigite nanoparticles.

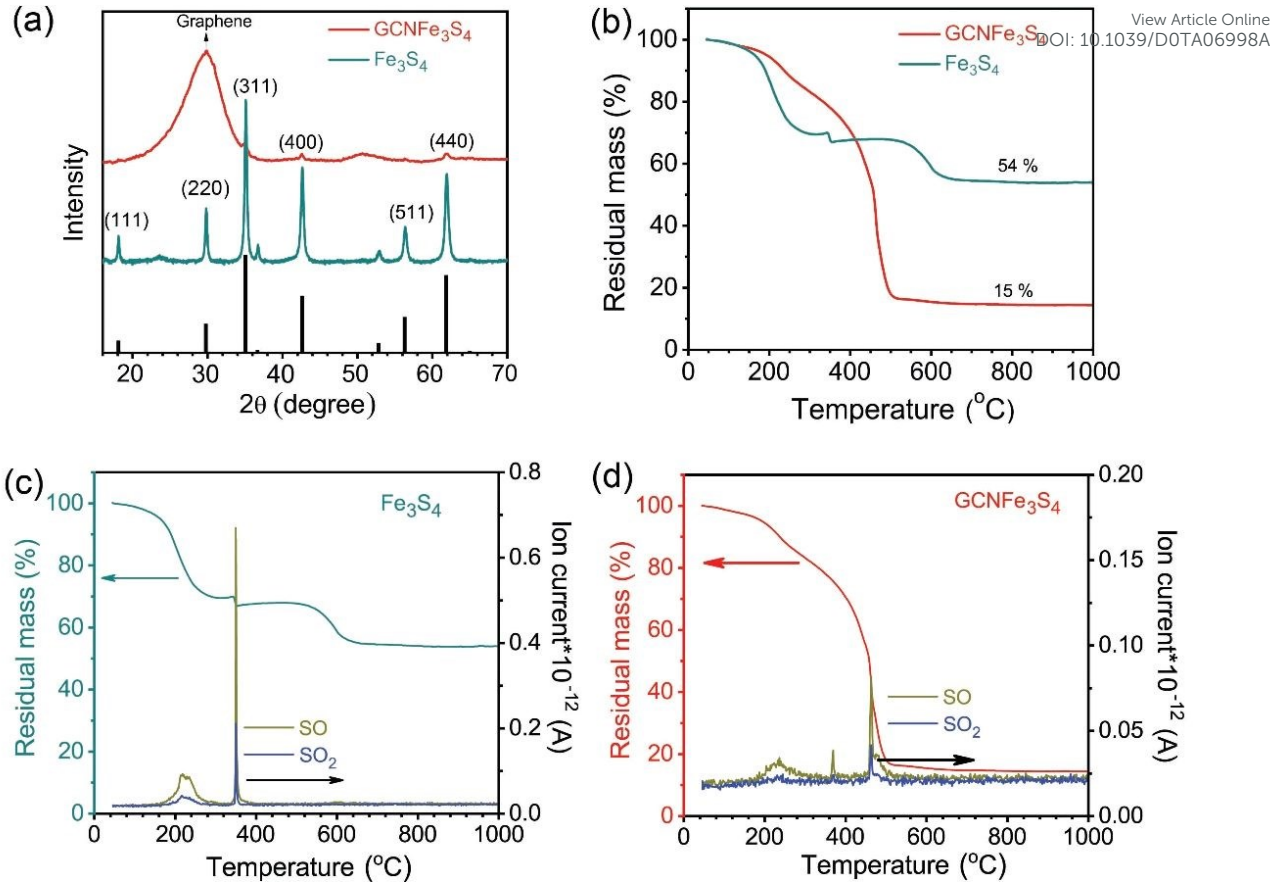


**Fig. 3**. (a) X-ray diffraction (Co-Kα radiation) for $GCNFe_3S_4$ and bare $Fe_3S_4$. The (*hkl)* planes for $Fe_3S_4$ appear as bars, adopted from ICDD 04-007-9796. (b) Thermogram under air for the $GCNFe_3S_4$ hybrid and for bare $Fe_3S_4$. Thermogram and evolved gas analysis for (c) $Fe_3S_4$, and (d) the $GCNFe_3S_4$ hybrid.

### 3.2. Electrochemical characterization

The electrochemical performance of the $GCNFe_3S_4$ hybrid and of its individual components were screened in a three-electrode half-cell configuration, in aqueous 1 M $Na_2SO_4$ electrolyte (Fig. 4a). Although the pure $Fe_3S_4$ was almost inactive in comparison to GCN, the area under the i/E curve (the capacitance) doubled for the $GCNFe_3S_4$ case, suggesting that the greigite was activated after its incorporation in the GCN. The small distortion of the cyclic voltammogram of $GCNFe_3S_4$ (deviation from a rectangular shape in comparison to than of pure GCN, Fig. 4a) also indicated the presence of fast redox reactions.[60] This could be attributed to the much smaller particle size and its seamless integration to the conductive GCN

View Article Online
DOI: 10.1039/D0TA06998A





support. We cannot rule out that a pillaring effect from the TMS nanoparticles, which mitigates the restacking of the graphene sheets, might also contribute to some extent for the observed increase in the capacitance after hybridization of GCN with $Fe_3S_4$. The performance was also evaluated in the widely used for iron sulfides KOH aqueous electrolyte (Fig. S5, ESI†), which delivered a specific capacitance of 104 $F \cdot g^{-1}$ at 1 A $g^{-1}$ and a specific energy of 9.4 $Wh \cdot kg^{-1}$ at a power of 0.8 $kW \cdot kg^{-1}$. These values were lower than several reported similar systems in the literature (Table S1, ESI†). We mainly attribute the higher performance of the reported systems to the direct growth of the active material on the current collectors (Table S1, ESI†). Nevertheless, such methods limit the potential for high-throughput electrode fabrication, because in these cases the current collectors must be present in the reaction vessel where the active materials are synthesized. Therefore, other approaches that may lead to similar or better performance, bypassing this limitation, are highly desirable.

Motivated by the typically poor wetting of TMS by water, the electrochemical response was explored in full cells with non-aqueous electrolytes (Fig. S3, ESI†). The highest response was achieved in the $EMIMBF_4$ ionic liquid electrolyte with LiTFSI additive (IL+LiTFSI, Fig. 4b), as suggested by the higher recorded specific currents (Fig. S3b, ESI†). Clear redox peaks could be observed, which were better resolved in the asymmetric cell of $GCNFe_3S_4$ against active carbon (Fig. S3c, ESI†). The anodic and cathodic peaks in the cyclic voltammograms showed a very small potential difference, which is the fingerprint of rapid pseudocapacitive and reversible redox processes, not involving phase changes of the electroactive material.[1] The cyclic voltammograms retained these key features both at low (Fig. S4, ESI†) and high scan rates (Fig. 4b). The fast and reversible electrochemistry of the $GCNFe_3S_4$ symmetric supercapacitor cell could be connected to the mixed-valence state of greigite, containing the basic structural motif of thiocubane $(Fe_2^{3+}Fe_2^{2+}S_4^{2-})^{2+}$, found in the active sites of ferredoxin

type enzymes.[61,62] In this unit, the oxidation states of $Fe^{2+}$ and $Fe^{3+}$ centers are not localized but shared among the octahedral $Fe^{3+}$ and $Fe^{2+}$ irons due to electron hopping, which enhances the conductivity. The mixed $Fe^{2+}/Fe^{3+}$ valence structure is also responsible for the unique triple redox-state of the unit,[63,64] thus allowing the effective charging-discharging of two identical electrodes from the resting $(Fe_2^{3+}Fe_2^{2+}S_4^{2-})^{2+}$ state to the oxidized $(Fe_3^{3+}Fe^{2+}S_4^{2-})^{3+}$ on the negative electrode and to the reduced $(Fe^{3+}Fe_3^{2+}S_4^{2-})^{1+}$ on the positive electrode. Interestingly, this is similar to the triple redox-state of the benchmark ultrafast pseudocapacitive, charge-storage material, $RuO_2$, as the Ru valence changes from $Ru^{4+}$ to $Ru^{3+}$ and $Ru^{2+}$.[38,54] $RuO_2$ is well-known for its capacitive-like cyclic voltammograms with subtle redox peaks due to the fast and fully reversible redox processes,[4,38,54] as in the present case. Nevertheless, its prohibitive high-cost and effective operation only in $H_2SO_4$ electrolytes have restricted its wide application. The X-ray photoelectron spectra of $GCNFe_3S_4$, after 10,000 charge/discharge cycles at 5 $A{\cdot}g^{-1}$, revealed only minor changes of the $Fe^{3+}/Fe^{2+/3+}$ ratio (from 0.33 to 0.48 after the cycling; Fig. S8, ESI†), verifying the stability of the observed redox processes in the cyclic voltammograms. Nevertheless, they also showed shifts of the Fe2p photoelectron peaks and changes of their widths, which along with the small $Fe^{3+}/ Fe^{2+/3+}$ ratio changes, suggest that the material has not been under a redox-resting state.

The galvanostatic charge-discharge curves were symmetric and linear (Fig. 4c), corroborating the observations from the cyclic voltammetry results,[65] and unveiled a very small internal resistance (IR-drop of 0.02 V and 0.04 V at 1 $A{\cdot}g^{-1}$, and 2 $A{\cdot}g^{-1}$, respectively), suggesting a very low equivalent series resistance, connected to the high rate capability.[26,65,66] Another key advantage of the IL+LiTFSI was the prevention of any sulfur losses from the ultrasmall greigite nanoparticles during the high-voltage cycling. Indicatively, when propylene carbonate was used, the cycling stability was poor (Fig. S6, ESI†), due to the dissolution of

View Article Online
DOI: 10.1039/D0TA06998A

sulfur or some sulfides/polysulfides in the organic solvent.[67,68] To verify this, the interaction of $GCNFe_3S_4$ with IL+LiTFSI was compared with that of propylene carbonate. The propylene carbonate clearly developed a yellowish color after the interaction (Fig. S7a, ESI†). Since the IL+LiTFSI has a similar yellowish color in its original state, the dissolution of sulfur was comparatively probed with photoluminescence mapping. The contamination of propylene carbonate was clearly evidenced by the spectral changes with maximum emission at 415 nm (excitation 350 nm; Fig. S7b-c, ESI†). On the contrary, the IL+LiTFSI fully retained its original properties with maximum emission at 450 nm (excitation: 380 nm, Fig. S7d-e, ESI†). As a result, the symmetric $GCNFe_3S_4$ cell displayed outstanding cycling stability, which was higher than the best-performing state-of-the-art TMS-based supercapacitors (Fig. 4d, and Table S1, ESI†). Initially, the capacitance increased up to 120% due to the electrochemical activation[29] of the electrode material by the gradual deeper and more effective electrolyte diffusion during charging/discharging, resulting into an increase of the stored charge. Even after 10,000 cycles at 5 $A \cdot g^{-1}$, the capacitance retention was 92% (Fig. 4d). Whereas, an $AC//Co_9S_8@C$ retained 86% of its capacitance after 10,000 cycles (Ref. [24]), and $FeS_2/GNS//Ni(OH)_2@Co_9S_8$ retained 86% after 5,000 cycles (Ref. [27]).

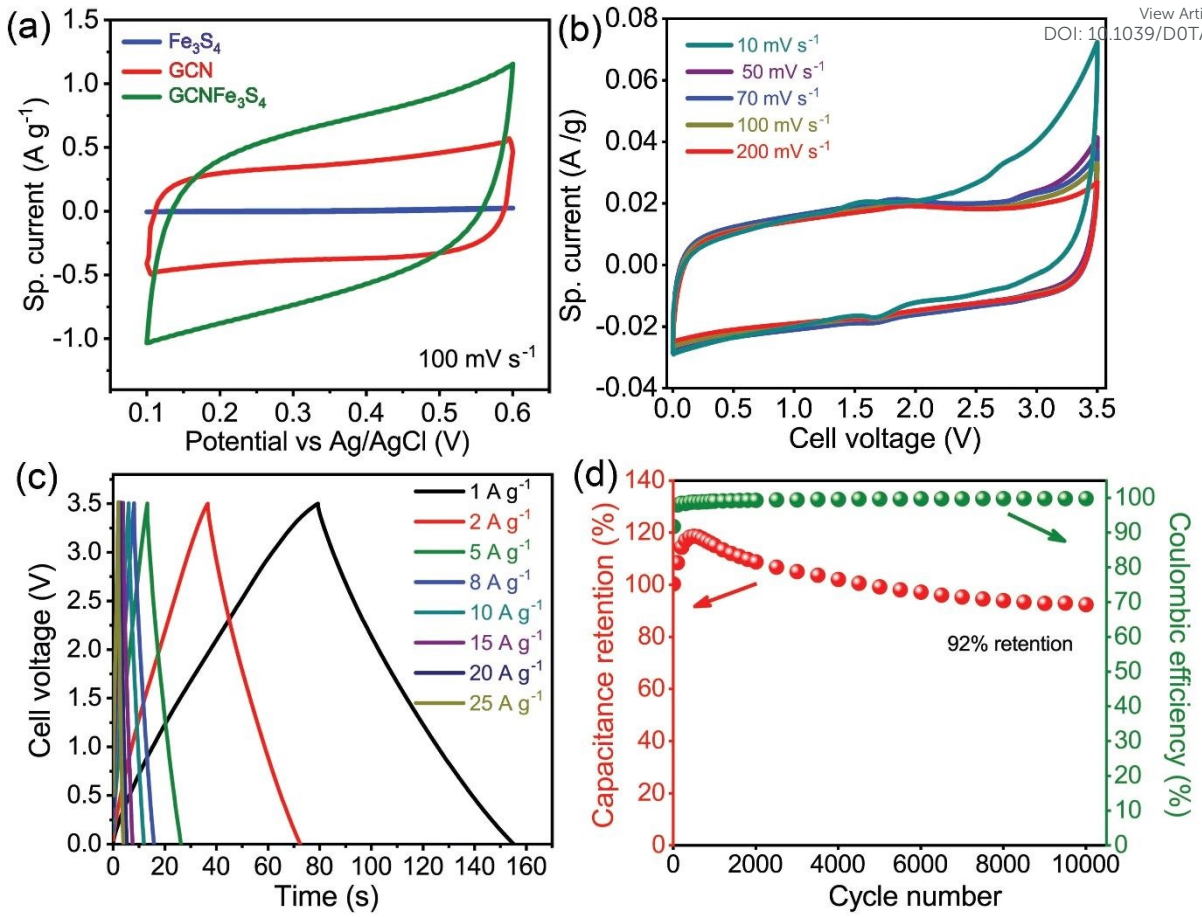


**Fig. 4**. (a) Cyclic voltammograms obtained for bare $Fe_3S_4$, GCN, and $GCNFe_3S_4$ hybrid at a scan rate of 100 mV·s$^{-1}$, using aqueous 1 M $Na_2SO_4$ in a three-electrode system. (b) Normalized to the scan rate cyclic voltammograms of the $GCNFe_3S_4$ hybrid obtained at various scan rates in a symmetric two-electrode full-cell of $GCNFe_3S_4$ in IL+LiTFSI, with the respective (c) galvanostatic charge/discharge curves obtained at 1-25 A·g$^{-1}$ and (d) cycling stability, and coulombic efficiency at 5 A·g$^{-1}$.

The specific capacitance obtained from the GCD curves in Fig. 4c was 88 $F \cdot g^{-1}$ at the specific current of 1 $A \cdot g^{-1}$ (Fig. 5a), which was retained by 72% up to a specific current of 25 $A \cdot g^{-1}$ (Fig. 5b), as anticipated from the low IR drop and fast redox kinetics. The excellent rate capability could be better understood through comparisons with previously reported full-cell supercapacitors based on TMS, as shown in Fig. 5c**,** and Table S1 (ESI†). For example, the AC//$Co_9S_8$@C (Ref. [24]) showed capacitance retention of 72% at a specific current of 18 $A \cdot g^{-1}$, and $NiFeS_2$/3DSG//3DSG (Ref. [69]) showed 70% capacitance retention at 10 A $g^{-1}$, although they were operated in aqueous electrolytes with much higher ionic conductivity. This result was obtained despite the use of commercial thin aluminum foil current collectors, instead of using Ni foams, which improve the electronic transport but have high mass density, affecting the true performance metrics negatively. The high rate-capability of GCN$Fe_3S_4$ was further supported by the Nyquist plot obtained from electrochemical impedance spectroscopy (EIS) in full-cell. The intersection of the plot with the real axis at the beginning of the high-frequency region corresponded to an equivalent series resistance ($R_s$) of 2.8 Ω before cycling (Fig. 5d, and Fig. S9, ESI†). The low $R_s$ values reflect the low electronic and ionic resistance of the material and the contact resistance with the current collector,[70] verifying the effective hybridization of GCN with $Fe_3S_4$. $R_s$ was only marginally increased to 3.3 Ω after 10,000 cycles (Fig. 5d, and Fig. S9, ESI†), corroborating the hybrid's stability upon cycling. It should be noted that the $R_s$ is slightly higher compared to other reports (such as the $R_s$ of 0.8 Ω for the half cell of $FeS_2$/GNS, Ref. [27]) because here, IL with a lower conductivity was used instead of water.[71,72]

In the high-frequency region in Fig. 5d, the absence of the semicircle indicated the very low charge transfer resistance($R_{ct}$) between the electrode and the electrolyte[70] (1.18 Ω as obtained by fitting the impedance spectra using the equivalent circuit shown in Fig. S9c, ESI†). This $R_{ct}$ was lower compared to the reported $R_{ct}$ of 1.3 Ω obtained for a carbon-supported

$Co_3S_4$ electrode measured in an aqueous electrolyte.[73] It was also significantly lower compared to that of pure $Fe_3S_4$ nanoparticles ($R_{ct}$ = 20.9 Ω) studied as Li-ion battery anode.[74] The inclined line at lower frequencies, approaching an angle of 90° against the real axis, indicated the fast ion diffusion in the bulk of the electrode.[72,75,76] The Bode/phase angle plots (calculated by fitting the Nyquist plots in Fig. S9a, ESI†), indicated a small drop from 75° to 70° after 10,000 charge/discharge cycles. The electrode with the high mass-loading after 10,000 cycles also showed a low $R_s$ (Fig. 5d) and a small reduction of the slope at low frequencies.

The specific capacitance of 88 $F \cdot g^{-1}$ at 1 $A \cdot g^{-1}$ corresponded to a specific energy of 37 $Wh \cdot kg^{-1}$ at a specific power of 2 $kW \cdot kg^{-1}$, which are important indicators for the performance of the cell.[1,39] Thus, it significantly surpassed both the energy and power which the same material delivered in the 6M KOH electrolyte, as previously discussed (9.4 $Wh \cdot kg^{-1}$ at 0.8 $kW \cdot kg^{-1}$). Furthermore, it retained an energy content of 25 $Wh \cdot kg^{-1}$ at a very high specific power of 35 $kW \cdot kg^{-1}$ (Table S2, ESI†). Therefore it surpassed many of the previously top-rated TMS-based electrode materials (Fig. 6a, and Table S1, ESI†).

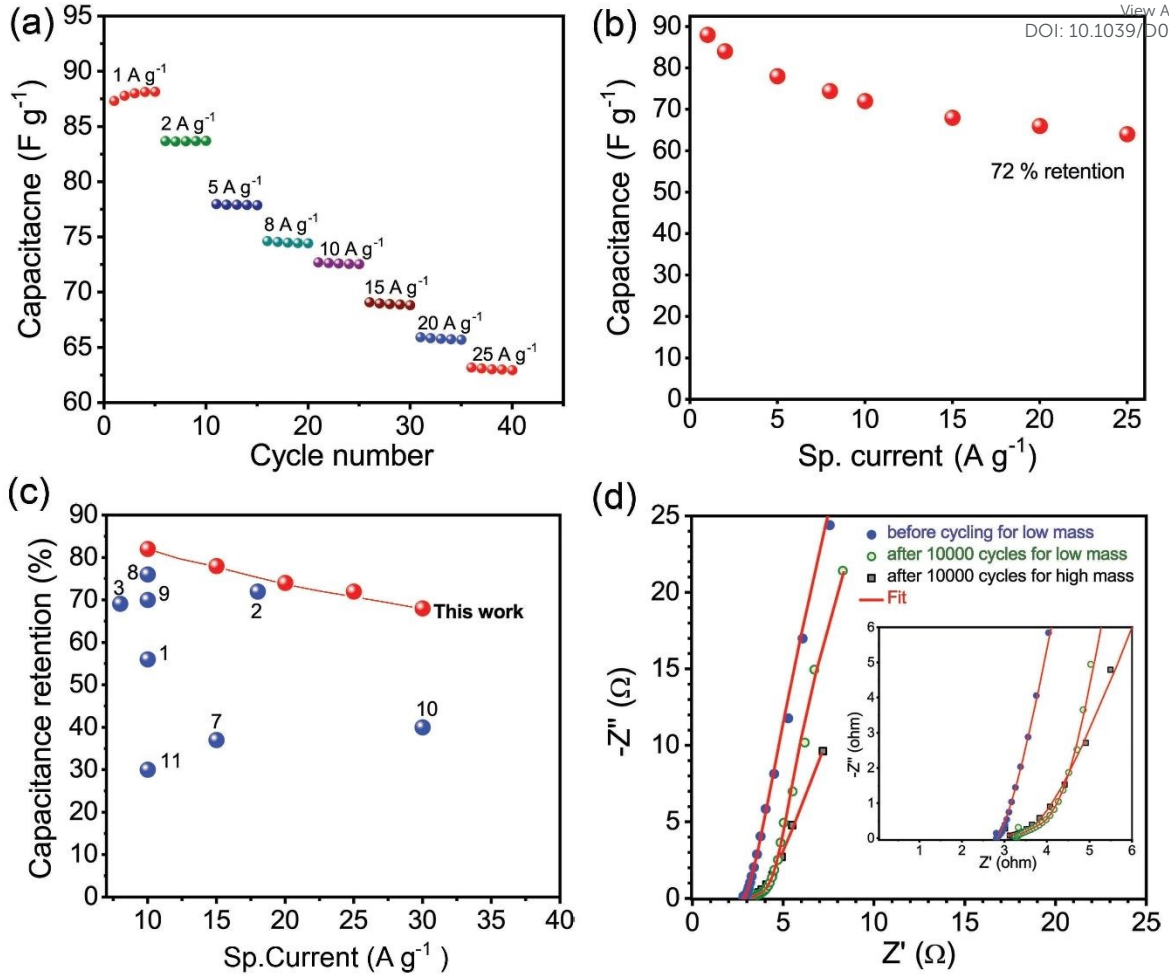


**Fig. 5**. (a) Rate performance at current densities from 1 A·g$^{-1}$ to 25 A·g$^{-1}$. (b) Specific capacitance retention at increasing specific current. (c) Comparison of the capacitance retention of GCNF$e_3S_4$ hybrid with respect to the state-of-the-art: (1) AC//$Co_9S_8$-NSA,[25] (2) AC//$Co_9S_8$@C,[24] (3) dr-$Bi_2S_3$/S-NCNF//S-NCNF,[28] (7) $FeS_2$/GNS//$Ni(OH)_2$@$Co_9S_8$,[27] (8) $rGO_{100}$-$CNT_{50}$-$Co_3S_4$//N-doped graphene,[73] (9) $NiFeS_2$/3DSG//3DSG,[69] (10) Fe-Co-S/NF//rGO,[77] (11) $CuCo_2O_4$/CuO//RGO/$Fe_2O_3$.[42] (d) Electrochemical impedance spectra of the GCNF$e_3S_4$ hybrid before and after electrochemical cycling.

To evaluate the materials closer to the true performance metrics,[78] we analyzed the results taking into account the mass of the current collectors. Accordingly, the performance comparison graph changed in favor of the GCNF$e_3S_4$ cell (Fig. 6b), which operated efficiently with the low areal mass-density commercial Al foil current collector. Therefore, the GCNF$e_3S_4$ symmetric supercapacitor surpassed the state-of-the-art in TMS supercapacitors and most of the oxide-based ones, apart from the record performance of the FeOOH-based system[15] (point 14 in Fig. 6b). Besides the promising performance, the chemistry and form of the GCNF$e_3S_4$ material is also compatible with the industrial roll-to-roll electrode coating techniques. This is in contrast to the systems that have to be synthesized and deposited on the current collectors during the synthesis reactions to achieve the required performance (i.e., the vast majority of the literature examples presented in Table S1, ESI†).

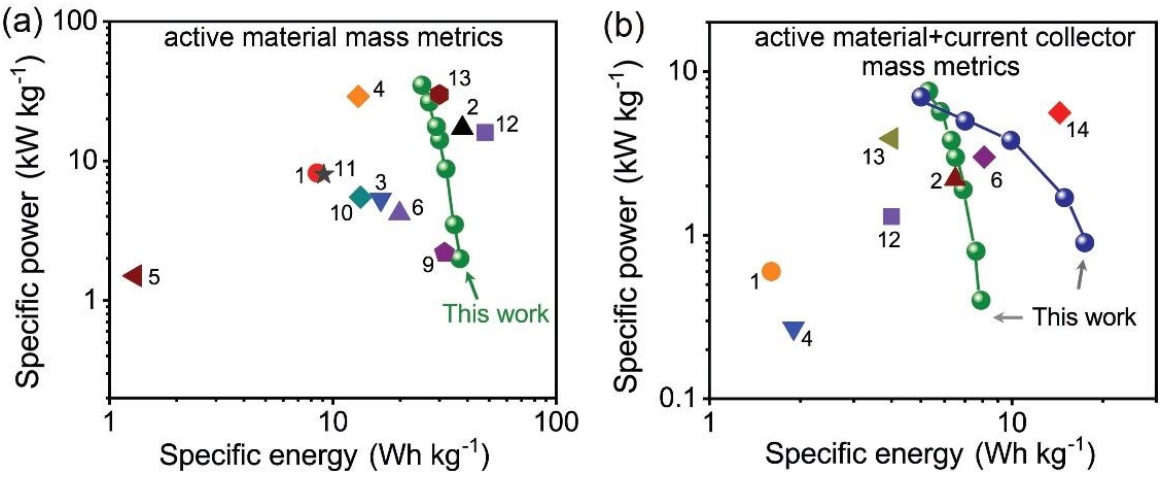


**Fig. 6**. Comparison of the specific energy and power for the GCNF$e_3S_4$ symmetric supercapacitor with state-of-the-art full cell supercapacitors based on metal sulfides and oxides. (a) Values reported at active mass level; (1) AC//$Co_9S_8$-NSA,[25] (2) AC//$Co_9S_8$@C,[24] (3) $Bi_2S_3$/S-NCNF//S-NCNF,[28] (4) $GCo_{0.33}Fe_{0.67}S_2$//SG-CoNiAl,[29] (5) $FeS_2$//$FeS_2$,[26] (6) rGO/FeS//$Ni(OH)_2$,[41] (7) $FeS_2$/GNS//$Ni(OH)_2$@$Co_9S_8$,[27] (9) $NiFeS_2$/3DSG//3DSG,[69] (10) Fe-Co-S/NF//rGO,[77] (11) $CuCo_2O_4$/CuO//RGO/$Fe_2O_3$,[16] (12) $Fe_2O_3$-QDs-3DGF//3DHPG,[42] and (13) $Mn_3O_4$//$Fe_3O_4$,[43] (b) Values reported at total electrode mass level, i.e.

View Article Online
DOI: 10.1039/D0TA06998A

including the mass of the current collectors (green spheres: mass loading of 0.9 mg·cm$^{-2}$; blue spheres: 3.5 mg·cm$^{-2}$); (14) FeOOH//$NiMoO_4$.[15] For details see Table S1, (ESI†).

For practical applications, the areal and volumetric performance is also of very high importance,[79] particularly regarding the micro-supercapacitors for wearable and on-chip electronics.[2,80,81] At a loading of 3.5 mg·cm$^{-2}$ (thickness 48 μm), the GCN$Fe_3S_4$ hybrid displayed a very high energy density of 49 mWh·cm$^{-3}$ at a very high power density 2.4 W·cm$^{-3}$ (Table S2, ESI†). Moreover, the GCN$Fe_3S_4$ cell could retain an energy density of 28 mWh·cm$^{-3}$ at a power of 11 W·cm$^{-3}$ (Table S2, ESI†). This volumetric performance is dramatically higher compared to the previously reported TMS-based supercapacitor cells of AC//$Cu_2O$–$Cu_{1.8}S$ (Ref. [45] with 2.1 mWh·cm$^{-3}$ at 0.031 W·cm$^{-3}$), and AC//HTMC-SCS-M (Ref. [46] with 3 mWh·cm$^{-3}$ at 0.77 mW·cm$^{-3}$). Regarding these volumetric characteristics, the present system surpassed many more top-rated materials, not only from the family of TMS. These include metal-like fluorine-doped *β*-FeOOH nanorods[47] and even some of the best carbon materials operating in high potential windows such as: carbon nanotubes with 47 mWh·cm$^{-3}$ at 1.4 W·cm$^{-3}$ (Ref. [49], using Pt mesh current collectors for boosting performance); doped carbon nanosheets with 42 mWh·cm$^{-3}$ at 0.4 W·cm$^{-3}$ (Ref. [50]); pillared graphene with 19.5 mWh·cm$^{-3}$ at 9 W·cm$^{-3}$ (Ref. [51]); dense graphene networks with 43 mWh·cm$^{-3}$ at 7.6 W·cm$^{-3}$ (Ref. [52]); and vertically aligned graphene sheets 6.5 mWh·cm$^{-3}$ at 2 W·cm$^{-3}$ (Ref.[48]). It is also indicative that the coconut-shell derived commercial activated carbon for supercapacitors (YP-80F), displays an energy density of 15 mWh·cm$^{-3}$ at 4.1 W·cm$^{-3}$.[52]

View Article Online
DOI: 10.1039/D0TA06998A



## 4. Conclusions

In this work, greigite ($Fe_3S_4$), with attractive redox chemistry due to its thiocubane basic structural unit of the communicating mixed-valence iron centers, was for the first time explored in a supercapacitor full-cell. Such transition metal sulfides have been dominantly studied in aqueous electrolytes to exploit the high charge transport in water and the $OH^-$ mediated redox chemistry. Nevertheless, we show that taking advantage of the hydrophobic nature of metal sulfides, a seamless hybrid between a highly functionalized graphene and ultrasmall $Fe_3S_4$ nanoparticles, prepared by a rapid, one-step method can deliver significant advantages in non-aqueous electrolytes. Owing to the firm immobilization on the conductive substrate, combined with the triple-redox state of greigite and its ultrasmall size, very fast and reversible redox processes were recorded even at high specific currents and up to 10,000 cycles, ascribing high rate capability and stability. The effective redox operation in the high voltage stability ionic liquid electrolyte ascribed a charge storage capability which surpassed the state-of-the-art systems in the field of metal sulfide supercapacitors, in terms of specific energy while keeping high specific power, as well as regarding the rate capability, despite the operation in an ionic liquid electrolyte. The volumetric performance surpassed the values even of top-rated materials from the broader range of supercapacitor materials. Importantly, this was achieved without the need of using direct growth of the active material on high mass-density current collectors, thus keeping the compatibility with high-throughput electrode fabrication processes. The present findings open a new direction regarding both the synthesis and the operation of such TMS-based supercapacitor cells toward further future developments.

View Article Online
DOI: 10.1039/D0TA06998A

**Electronic supplementary information (ESI)**

X-ray photoelectron emission spectra, thermograms and evolved gas analysis results, supporting electrochemical data (cyclic voltammetry, galvanostatic charge/discharge profiles, stability plots, electrochemical impedance spectra), comparative tables with performance values.

**Acknowledgments**

The authors acknowledge the support by the Operational Program Research, Development and Education–European Regional Development Fund, Project No. CZ.02.1.01/0.0/0.0/16_019/0000754 of the Ministry of Education, Youth and Sports of the Czech Republic, the Internal Grant Agency (IGA) of the Palacký University in Olomouc (Project No. IGA_PrF_2020_011 and No. IGA_PrF_2020_022). V.P. thanks Eduard Arzt (INM) for continuing support. Tomáš Steklý (cyanographene preparation), Jana Stráska (TEM), Martin Petr (XPS), Dr. Claudia Aparicio and Dr. Josef Kašlík (XRD), Dr. Juri Ugolotti and Jana Havláková (TGA and EGA) are acknowledged for the measurements. M.O. thanks H2020 ERC project 683024. A.B and R.Z thank Czech Science Foundation, project GA CR – EXPRO, 19-27454X.

## References


1 V. Augustyn, P. Simon and B. Dunn, *Energy Environ. Sci.*, 2014, **7**, 1597–1614.
2 C. Zhang, W. Lv, Y. Tao and Q.-H. Yang, *Energy Environ. Sci.*, 2015, **8**, 1390–1403.
3 S. Fleischmann, J. B. Mitchell, R. Wang, C. Zhan, D. Jiang, V. Presser and V. Augustyn, *Chem. Rev.*, 2020, **14**, 6738–6782.
4 E. Frackowiak and F. Béguin, *Carbon*, 2001, **39**, 937–950.
5 P. Simon, Y. Gogotsi and B. Dunn, *Science*, 2014, **343**, 1210–1211.
6 D. P. Dubal, K. Jayaramulu, R. Zboril, R. A. Fischer and P. Gomez-Romero, *J. Mater. Chem. A*, 2018, **6**, 6096–6106.
7 A. Bakandritsos, D. D. Chronopoulos, P. Jakubec, M. Pykal, K. Čépe, T. Steriotis, S. Kalytchuk, M. Petr, R. Zbořil and M. Otyepka, *Adv. Funct. Mater.*, 2018, **28**, 1801111.
8 Y. Kim, T. Park, J. Na, J. W. Yi, J. Kim, M. Kim, Y. Bando, Y. Yamauchi and J. Lin, *Nanoscale*, 2020, **12**, 8608–8625.
9 F. Bonaccorso, L. Colombo, G. Yu, M. Stoller, V. Tozzini, A. C. Ferrari, R. S. Ruoff and V. Pellegrini, *Science*, 2015, **347**, 1246501.
10 Y. Ji, L. Huang, J. Hu, C. Streb and Y.-F. Song, *Energy Environ. Sci.*, 2015, **8**, 776–789.
11 F. Yi, H. Ren, J. Shan, X. Sun, D. Wei and Z. Liu, *Chem. Soc. Rev.*, 2018, **47**, 3152–3188.
12 V. Georgakilas, J. A. Perman, J. Tucek and R. Zboril, *Chem. Rev.*, 2015, **115**, 4744–4822.
13 V. Georgakilas, J. N. Tiwari, K. C. Kemp, J. A. Perman, A. B. Bourlinos, K. S. Kim and R. Zboril, *Chem. Rev.*, 2016, **116**, 5464–5519.
14 S. V. Talande, A. Bakandritsos, P. Jakubec, O. Malina, R. Zbořil and J. Tuček, *Adv. Funct. Mater.*, 2019, **27**, 1906998.
15 K. A. Owusu, L. Qu, J. Li, Z. Wang, K. Zhao, C. Yang, K. M. Hercule, C. Lin, C. Shi, Q. Wei, L. Zhou and L. Mai, *Nat. Commun.*, 2017, **8**, 14264.
16 Y. Wang, C. Shen, L. Niu, R. Li, H. Guo, Y. Shi, C. Li, X. Liu and Y. Gong, *J. Mater. Chem. A*, 2016, **4**, 9977–9985.
17 T. Gu and B. Wei, *J. Mater. Chem. A*, 2016, **4**, 12289–12295.
18 D. P. Dubal, K. Jayaramulu, J. Sunil, Š. Kment, P. Gomez-Romero, C. Narayana, R. Zbořil and R. A. Fischer, *Adv. Funct. Mater.*, 2019, **29**, 1900532.
19 C. Zhao, X. Shao, Y. Zhang and X. Qian, *ACS Appl. Mater. Interfaces*, 2016, **8**, 30133–30142.
20 Q. Lv, S. Wang, H. Sun, J. Luo, J. Xiao, J. Xiao, F. Xiao and S. Wang, *Nano Lett.*, 2016, **16**, 40–47.
21 C. Huang, Y. Li, N. Wang, Y. Xue, Z. Zuo, H. Liu and Y. Li, *Chem. Rev.*, 2018, **118**, 7744–7803.
22 Y. Xue, B. Huang, Y. Yi, Y. Guo, Z. Zuo, Y. Li, Z. Jia, H. Liu and Y. Li, *Nat. Commun.*, 2018, **9**, 1460.
23 L. Li, Z. Zuo, F. Wang, J. Gao, A. Cao, F. He and Y. Li, *Adv. Mater.*, 2020, **32**, 2000140.
24 S. Sun, J. Luo, Y. Qian, Y. Jin, Y. Liu, Y. Qiu, X. Li, C. Fang, J. Han and Y. Huang, *Adv. Energy Mater.*, 2018, **8**, 1801080.
25 X. Han, K. Tao, D. Wang and L. Han, *Nanoscale*, 2018, **10**, 2735–2741.
26 S. Venkateshalu, P. Goban Kumar, P. Kollu, S. K. Jeong and A. N. Grace, *Electrochimica Acta*, 2018, **290**, 378–389.
27 Z. Sun, H. Lin, F. Zhang, X. Yang, H. Jiang, Q. Wang and F. Qu, *J. Mater. Chem. A*, 2018, **6**, 14956–14966.
28 W. Zong, F. Lai, G. He, J. Feng, W. Wang, R. Lian, Y.-E. Miao, G.-C. Wang, I. P. Parkin and T. Liu, *Small*, 2018, **14**, 1801562.
29 W. Liu, H. Niu, J. Yang, K. Cheng, K. Ye, K. Zhu, G. Wang, D. Cao and J. Yan, *Chem. Mater.*, 2018, **30**, 1055–1068.
30 C. Jing, X. Guo, L. Xia, Y. Chen, X. Wang, X. Liu, B. Dong, F. Dong, S. Li and Y. Zhang, *Chem. Eng. J.*, 2020, **379**, 122305.
31 N. Choudhary, C. Li, H.-S. Chung, J. Moore, J. Thomas and Y. Jung, *ACS Nano*, 2016, **10**, 10726–10735.
32 P. Geng, S. Zheng, H. Tang, R. Zhu, L. Zhang, S. Cao, H. Xue and H. Pang, *Adv. Energy Mater.*, 2018, **8**, 1703259.

33 X. Wang, Q. Zhang, J. Sun, Z. Zhou, Q. Li, B. He, J. Zhao, W. Lu, C. Wong and Y. Yao, *J. Mater. Chem. A*, 2018, **6**, 8030–8038.
34 N. Li, Z. Weng, Y. Wang, F. Li, H.-M. Cheng and H. Zhou, *Energy Environ. Sci.*, 2014, **7**, 3307–3312.
35 Z. Li, M. Chen, P. Huang, Q. Zhang and S. Song, *Trans. Nonferrous Met. Soc. China*, 2017, **27**, 2474–2480.
36 J. Wang, J. Lu, Q. Zhang and F. Saito, *Ind. Eng. Chem. Res.*, 2003, **42**, 5813–5818.
37 M. J. Russell and A. J. Hall, *The onset and early evolution of life*, Geological Society of America, 2006.
38 M. Salanne, B. Rotenberg, K. Naoi, K. Kaneko, P.-L. Taberna, C. P. Grey, B. Dunn and P. Simon, *Nat. Energy*, 2016, **1**, 201670.
39 P. Simon and Y. Gogotsi, *Nat. Mater.*, 2008, **7**, 845–854.
40 X. Rui, H. Tan and Q. Yan, *Nanoscale*, 2014, **6**, 9889–9924.
41 C. Zhao, X. Shao, Z. Zhu, C. Zhao and X. Qian, *Electrochimica Acta*, 2017, **246**, 497–506.
42 Y. Li, H. Zhang, S. Wang, Y. Lin, Y. Chen, Z. Shi, N. Li, W. Wang and Z. Guo, *J. Mater. Chem. A*, 2016, **4**, 11247–11255.
43 J. W. Choi, I. W. Ock, K.-H. Kim, H. M. Jeong and J. K. Kang, *Adv. Funct. Mater.*, 2018, **28**, 1803695.
44 S. Sun, J. Lang, R. Wang, L. Kong, X. Li and X. Yan, *J. Mater. Chem. A*, 2014, **2**, 14550–14556.
45 A. Esfandiar, M. Qorbani, I. Shown and B. O. Dogahe, *J. Mater. Chem. A*, 2020, **8**, 1920–1928.
46 Y.-W. Lee, B.-S. Kim, J. Hong, H. Choi, H.-S. Jang, B. Hou, S. Pak, J. Lee, S.-H. Lee, S. M. Morris, D. Whang, J.-P. Hong, H. S. Shin, S. Cha, J. I. Sohn and J. M. Kim, *Nano Energy*, 2017, **37**, 15–23.
47 L.-F. Chen, Z.-Y. Yu, J.-J. Wang, Q.-X. Li, Z.-Q. Tan, Y.-W. Zhu and S.-H. Yu, *Nano Energy*, 2015, **11**, 119–128.
48 Y. Yoon, K. Lee, S. Kwon, S. Seo, H. Yoo, S. Kim, Y. Shin, Y. Park, D. Kim, J.-Y. Choi and H. Lee, *ACS Nano*, 2014, **8**, 4580–4590.
49 A. Izadi-Najafabadi, S. Yasuda, K. Kobashi, T. Yamada, D. N. Futaba, H. Hatori, M. Yumura, S. Iijima and K. Hata, *Adv. Mater.*, 2010, **22**, E235–E241.
50 J. Hou, C. Cao, F. Idrees and X. Ma, *ACS Nano*, 2015, **9**, 2556–2564.
51 F.-G. Zhao, Y.-T. Kong, B. Pan, C.-M. Hu, B. Zuo, X. Dong, B. Li and W.-S. Li, *J. Mater. Chem. A*, 2019, **7**, 3353–3365.
52 P. Li, H. Li, D. Han, T. Shang, Y. Deng, Y. Tao, W. Lv and Q.-H. Yang, *Adv. Sci.*, 2019, **6**, 1802355.
53 A. Bakandritsos, M. Pykal, P. Błoński, P. Jakubec, D. D. Chronopoulos, K. Poláková, V. Georgakilas, K. Čépe, O. Tomanec, V. Ranc, A. B. Bourlinos, R. Zbořil and M. Otyepka, *ACS Nano*, 2017, **11**, 2982–2991.
54 C. Choi, D. S. Ashby, D. M. Butts, R. H. DeBlock, Q. Wei, J. Lau and B. Dunn, *Nat. Rev. Mater.*, 2020, **5**, 5–19.
55 Y. Yang, H. Fei, G. Ruan, C. Xiang and J. M. Tour, *Adv. Mater.*, 2014, **26**, 8163–8168.
56 A. Paolella, C. George, M. Povia, Y. Zhang, R. Krahne, M. Gich, A. Genovese, A. Falqui, M. Longobardi, P. Guardia, T. Pellegrino and L. Manna, *Chem. Mater.*, 2011, **23**, 3762–3768.
57 X. Zhao, X. Lan, D. Yu, H. Fu, Z. Liu and T. Mu, *Chem. Commun.*, 2018, **54**, 13010–13013.
58 T. Gao, S. Hou, F. Wang, Z. Ma, X. Li, K. Xu and C. Wang, *Angew. Chem. Int. Ed.*, 2017, **56**, 13526–13530.
59 K. Igarashi, Y. Yamamura and T. Kuwabara, *Geochim. Cosmochim. Acta*, 2016, **191**, 47–57.
60 N. H. N. Azman, M. S. M. @ M. Nazir, L. H. Ngee and Y. Sulaiman, *Int. J. Energy Res.*, 2018, **42**, 2104–2116.
61 A. Roldan, N. Hollingsworth, A. Roffey, H.-U. Islam, J. B. M. Goodall, C. R. A. Catlow, J. A. Darr, W. Bras, G. Sankar, K. B. Holt, G. Hogarth and N. H. de Leeuw, *Chem. Commun.*, 2015, **51**, 7501–7504.
62 M. J. Russell, R. M. Daniel, A. J. Hall and J. A. Sherringham, *J. Mol. Evol.*, 1994, **39**, 231–243.
63 P. Venkateswara Rao and R. H. Holm, *Chem. Rev.*, 2004, **104**, 527–560.
64 D. Benício, *Bioinorganic Chemistry*, University Science Book, Mill Valley, California, 1994.
65 R. Wang and X. Yan, *Sci. Rep.*, 2014, **4**, 1–9.
66 X. Ye, Y. Zhu, H. Jiang, L. Wang, P. Zhao, Z. Yue, Z. Wan and C. Jia, *Chem. Eng. J.*, 2019, **361**, 1437–1450.
67 W.-J. Yu, C. Liu, L. Zhang, P.-X. Hou, F. Li, B. Zhang and H.-M. Cheng, *Adv. Sci.*, 2016, **3**, 1600113.

View Article Online
DOI: 10.1039/D0TA06998A

68 Y. Zhu, X. Fan, L. Suo, C. Luo, T. Gao and C. Wang, *ACS Nano*, 2016, **10**, 1529–1538.
69 T. Ma, H. Liu, Y. Wang and M. Zhang, *Electrochimica Acta*, 2019, **309**, 1–10.
70 S. Chandra Sekhar, G. Nagaraju and J. S. Yu, *Nano Energy*, 2018, **48**, 81–92.
71 Y. Shao, M. F. El-Kady, J. Sun, Y. Li, Q. Zhang, M. Zhu, H. Wang, B. Dunn and R. B. Kaner, *Chem. Rev.*, 2018, **118**, 9233–9280.
72 G. Wang, L. Zhang and J. Zhang, *Chem. Soc. Rev.*, 2012, **41**, 797–828.
73 A. Mohammadi, N. Arsalani, A. G. Tabrizi, S. E. Moosavifard, Z. Naqshbandi and L. S. Ghadimi, *Chem. Eng. J.*, 2018, **334**, 66–80.
74 T. Li, H. Li, Z. Wu, H. Hao, J. Liu, T. Huang, H. Sun, J. Zhang, H. Zhang and Z. Guo, *Nanoscale*, 2015, **7**, 4171–4178.
75 J. Chen, J. Xu, S. Zhou, N. Zhao and C.-P. Wong, *Nano Energy*, 2016, **21**, 145–153.
76 Q. X. Low and G. W. Ho, *Nano Energy*, 2014, **5**, 28–35.
77 K. Le, M. Gao, W. Liu, J. Liu, Z. Wang, F. Wang, V. Murugadoss, S. Wu, T. Ding and Z. Guo, *Electrochimica Acta*, 2019, **323**, 134826.
78 Y. Gogotsi and P. Simon, *Science*, 2011, **334**, 917–918.
79 M. D. Stoller and R. S. Ruoff, *Energy Environ. Sci.*, 2010, **3**, 1294–1301.
80 W. Gu and G. Yushin, *WIREs Energy Environ.*, 2014, **3**, 424–473.
81 D. Yu, K. Goh, H. Wang, L. Wei, W. Jiang, Q. Zhang, L. Dai and Y. Chen, *Nat. Nanotechnol.*, 2014, **9**, 555–562.

View Article Online
DOI: 10.1039/D0TA06998A



## Table of Contents Entry

**Integrating thiocubane's redox chemistry with a highly functionalized graphene in a non-aqueous electrolyte supercapacitor boosts energy and power density.**